Ultrasound Calibration Framework for the Image-Guided Surgery Toolkit (IGSTK)

Ziv Yaniv[a], Pezhman Foroughi[b], Hyun-Jae Kang[b], and Emad Boctor[b,c]

[a]Imaging Science and Information Systems (ISIS) Center, Dept. of Radiology, Georgetown University Medical Center, Washington, DC,USA
[b]Department of Computer Science,Johns Hopkins University, Baltimore, USA
[c]Department of Radiology,Johns Hopkins University, Baltimore, USA

ABSTRACT

Registration is a key technology in image-guided navigation systems. By aligning pre-operative images with the intra-operative setting these systems provide visual feedback that improves the physician's understanding of the spatial relationships between anatomical structures and surgical tools. Most often the alignment is obtained using fiducials. Another option is to replace the use of fiducials with intra-operative imaging. Two dimensional ultrasound (US) is a widely available intra-operative non-ionizing imaging modality. To utilize this modality for registration one must first perform spatial calibration of the US. In this work we describe the implementation of three spatial calibration methods as part of the image-guided surgery toolkit (IGSTK). The implementation follows the IGSTK calibration framework, separating algorithmic aspects from user interaction aspects of the calibration. Our calibration framework includes three methods. The first is a phantom-less method using a tracked pointer tool in addition to the tracked US, the second method uses a cross-wire phantom, and the third method is based on the use of a plane phantom.

Keywords: image-guided therapy, ultrasound calibration, open source software

1. INTRODUCTION

Two dimensional ultrasound (US) is a ubiquitous non-ionizing intra-operative imaging modality. In the context of image-guided interventions it has been primarily used for registration purposes, alignment of pre-operative imaging with the intra-operative patient space. This use is motivated by the desire to reduce the patients' and medical staff's exposure to ionizing radiation associated with the intra-operative use of x-ray imaging. In addition, while most US images are two dimensional (2D), they do not compound spatial data into a single image as is the case with x-ray projections. As a consequence once a 2D US system is spatially calibrated it readily provides three dimensional (3D) information which can be used for registration. These US systems are known as freehand 3D US.

In image-guided interventions they have been utilized for a variety of registration applications. Among others these include, rigid US to CT registration of a single vertebral body,[1] group wise rigid US to CT registration of multiple vertebral bodies using biomechanical constraints,[2] model instantiation and rigid registration of US to a CT based atlas[3] of the femur and pelvis, rigid and affine registration of US to CT of the liver,[4,5] and for rigid registration of US elastography images to a CT of the kidney.[6] The prerequisite for all of these uses is spatial calibration.

Spatial calibration of 2D US systems has been addressed using two primary approaches, phantom based calibration methods and combination of 3D registration and calibration.[7] The majority of calibration methods use phantoms. These phantoms have varying degrees of complexity, from simple objects such as the planar bottom of a water bath[8] to complex phantoms such as the Hopkins phantom.[9]

We are currently implementing an US calibration framework as part of the Image-Guided Surgery Toolkit (IGSTK).[10] IGSTK is a free open source C++ toolkit providing a framework for rapid development of customized image-guidance applications. The toolkit provides a set of components common to most navigation systems.

E-mail: zivy@isis.georgetown.edu

Medical Imaging 2011: Visualization, Image-Guided Procedures, and Modeling, edited by Kenneth H. Wong, David R. Holmes III, Proc. of SPIE Vol. 7964, 79641N

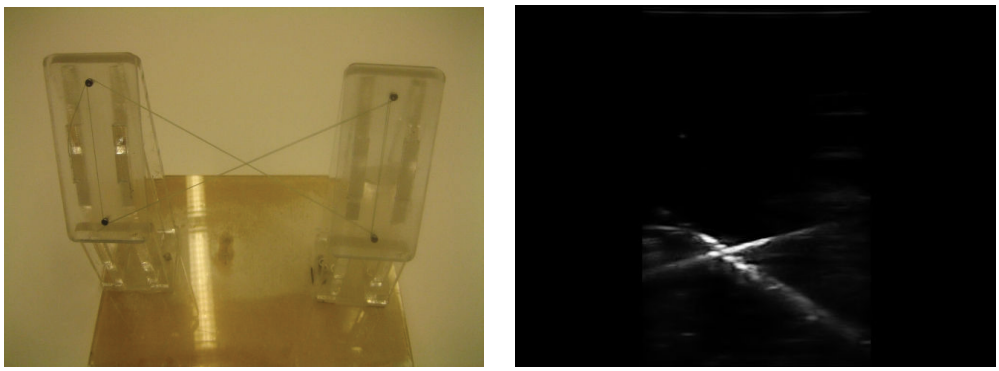

Figure 1. Experimental setup for the cross-wire phantom evaluation and sample image.

Currently, these include: 1) interfaces to various tracking devices; 2) DICOM image readers; 3) paired-point rigid body registration; 4) visualization components; and 5) an internal logging mechanism. We are extending the toolkit to include various calibration algorithms used in image-guided navigation procedures. The current release, 4.2., of the toolkit includes an implementation of pivot-calibration, localizing the tip of a pointer tool with respect to its dynamic reference frame (DRF). Spatial calibration of 2D US is expected to be available in the next release of the toolkit.

We next describe in detail the US calibration algorithms, the IGSTK calibration framework, and an initial evaluation of the implementation.

2. MATERIALS AND METHODS

We have implemented three phantom based spatial calibration methods. The first method requires the least amount of hardware, using the planar bottom of a water bath as the calibration phantom.[8] The second method utilizes a tracked calibrated pointer.[11] This method is often referred to as phantom-less, a bit of a misnomer as the pointer tip locations serve as a virtual multi-point phantom. The third method we implement is closely related to the previous one. This is the cross-wire based method.[12]

To enable robust estimation of the calibration parameters we use a generic implementation of the Random Sample Consensus (RANSAC) algorithm.[13] This allows us to perform robust estimation without integrating the RANSAC algorithm into each of the calibration methods. Implementation details and example source code for that algorithm are given in.[14] To utilize the RANSAC algorithm we require: 1) a method for parameter estimation using the minimal number of data elements, usually an analytic estimate; 2) a method for least squares parameter estimation; and 3) a method that checks if a data element agrees with specific model parameter values, in our case the point to plane distance or the distance between corresponding points. Appendices A and B describe these elements for our calibration algorithms.

The IGSTK architecture supports the use of pre-operatively estimated transforms using three independent layers. At the most basic level the toolkit provides components for reading and writing transformations using the XML file format. Currently the supported transformation types include, rigid, affine, and perspective. The second layer of support includes components that encapsulate transformation estimation algorithms, currently these include rigid paired-point based registration and pivot calibration of a tracked pointer probe. This layer of support also includes components that facilitate data acquisition, allowing the user to start and stop image and tracking data gathering. Finally the third top layer includes UI components that use the data acquisition and algorithmic components to provide turn-key solutions for transformation estimation. Our current work adds components to the second layer, support for three US calibration algorithms.

A key feature of IGSTK is the use of state machines to ensure safety. While this is crucial in medical applications it has its drawbacks. Primarily, the architecture is cumbersome for algorithmic development. As a consequence we have implemented our algorithms as an external library. IGSTK components provide access to the algorithms via encapsulation. This is similar to the current support of paired-point rigid registration where the IGSTK component encapsulates the algorithm implementation from the Insight Toolkit (ITK).[15]

```
<?xml version="1.0" encoding="ISO-8859-1"?>

<precomputed_transform>

        <description>
        US calibration - Crosswire Phantom
        </description>

        <computation_date>
        2011 Jan 16 15:47:28
        </computation_date>

         <transformation estimation_error="0.4281934697">
        0.1538730166        -0.0058332995        0.0013026667        -92.1328221666
        -0.0004171231        -0.0056774548        0.9993122957        -1.3737261672
        -0.0058393730        -0.1533074177        -0.0370572362        -33.3226485357
        </transformation>

</precomputed_transform>
```

Table 1. Example XML file.

We empirically evaluated our implementation of the cross-wire calibration algorithm. The experimental setup is shown in Figure 1. Tracking data was acquired with the Polaris hybrid system from Northern Digital Inc. (Waterloo, Ontario, Canada). Images were acquired using the Sonix CEP ultrasound machine from Ultrasonix Medical Corporation (Richmond, BC, Canada), via the system's Porta API. API. Data acquisition was performed by three operators and the variability of the calibration was evaluated. Our measure of variability is the distance between corresponding image points transformed to the DRF coordinate system attached to the US. We use all image points in this evaluation.

3. EXPERIMENTAL RESULTS

Three calibration results were obtained for the cross-wire phantom. The results were saved in the IGSTK XML file format. A sample is shown in Table 1.

When comparing the calibration results for all operators we obtained a median difference between transformed points of 3.06mm with a standard deviation of 1.49mm. It is interesting to note that for one of the three operators this was the first calibration session using this type of phantom. This is reflected by the smaller difference between the two other operators, median of 2.05mm and standard deviation of 0.45mm. The difference distribution for all three operators and for the two experienced operators is shown in Figure 2.

4. DISCUSSION AND CONCLUSIONS

Two dimensional US is a ubiquitous non-ionizing intra-operative imaging modality. In the context of image-guided interventions it has been primarily used for registration purposes. A prerequisite for this usage is US calibration, relating the image coordinates to a tracked reference frame rigidly attached to the ultrasound probe.

We have implemented three calibration algorithms as part of the Image-Guided Surgery Toolkit's calibration framework. To improve their robustness to outliers we use a generic implementation of the RANSAC algorithm. This enables each of the calibration estimators to utilize this robust estimation algorithm without explicitly incorporating it into the specific implementation.

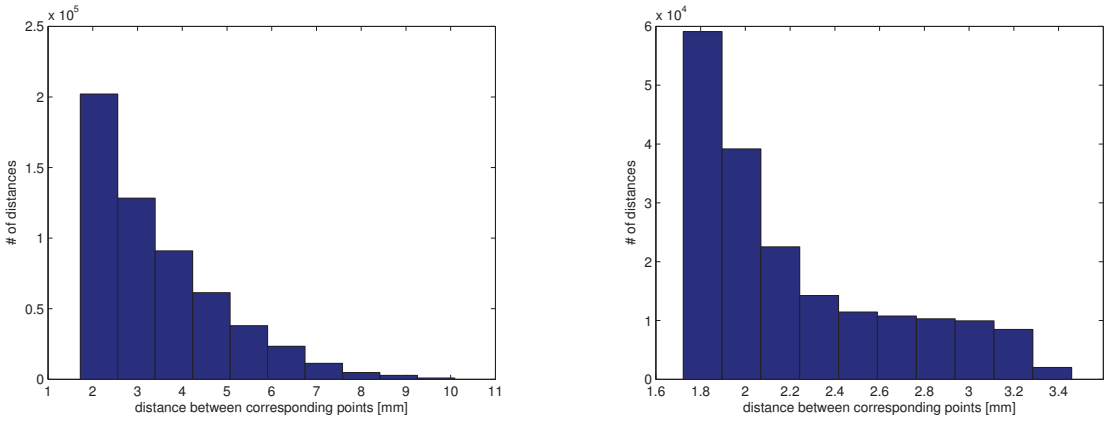

(a) (b)

Figure 2. Histograms of distances between corresponding image points after applying the calibration transformation (a) for all three operators (b) for the two experienced operators. Note that the histograms have different scales.

Finally, we evaluated the variability of the cross-wire calibration procedure using our implementation. Not surprisingly, we identified that data acquisition is a learned skill with more experienced operators being more consistent with each other as compared to a novice.

The open source implementation of these algorithms is available from two software repositories. The standard C++ implementation is available from a git repository. Clone the repository using the following command:

```
git clone https://github.com/zivy/LSQRRecipes.git LSQRRecipes
```

IGSTK wrappers are available on the toolkit's sandbox cvs repository. Download the sandbox repository using the following commands:

```
cvs d :pserver:anonymous@public.kitware.com:/cvsroot/IGSTK login
answer by 'igstk'
cvs -d :pserver:anonymous@public.kitware.com:/cvsroot/IGSTK co IGSTKSandbox
```

ACKNOWLEDGMENTS

This work is supported by NIH grant 5R01EB007195 (NIBIB). The content of this manuscript does not necessarily reflect the official views of the NIH.

REFERENCES

[1] Winter, S., Pechlivanis, I., Dekomien, C., Igel, C., and Schmieder, K., "Toward registration of 3D ultrasound and CT images of the spine in clinical praxis: Design and evaluation of data acquisition protocol," *Ult* **35**(11), 1773–1782 (2009).

[2] Gill, S., Abolmaesumi, P., Fichtinger, G., Boisvert, J., Pichora, D., Borshneck, D., and Mousavi, P., "Biomechanically constrained groupwise ultrasound to CT registration of the lumbar spine," *Medical Image Analysis* **In Press**, – (2011).

[3] Barratt, D. C., Chan, C. S., Edwards, P. J., Penney, G. P., Slomczykowski, M., Carter, T. J., and Hawkes, D. J., "Instantiation and registration of statistical shape models of the femur and pelvis using 3D ultrasound imaging," *Medical Image Analysis* **12**(3), 358–374 (2008).

[4] Wein, W., Brunke, S., Khamene, A., Callstrom, M. R., and Navab, N., "Automatic CT-ultrasound registration for diagnostic imaging and image-guided intervention," *Medical Image Analysis* **12**, 577–585 (2008).

[5] Penney, G., Blackall, J., Hamady, M., Sabharwal, T., Adam, A., and Hawkes, D., "Registration of freehand 3D ultrasound and magnetic resonance liver images," *Medical Image Analysis* **8**(1), 81–91 (2004).

[6] Stolka, P. J., Keil, M., Sakas, G., McVeigh, E., Allaf, M. E., Taylor, R. H., and Boctor, E. M., "A 3D-elastography-guided system for laparoscopic partial nephrectomies," in [*SPIE Medical Imaging*], (2010).

[7] Mercier, L., Langø, T., Lindseth, F., and Collins, D. L., "A review of calibration techniques for freehand 3-D ultrasound systems," *Ultrasound in Med. Biol.* **31**(4), 449–471 (2005).

[8] Prager, R. W., Rohling, R. N., Gee, A. H., and Berman, L., "Rapid calibration for 3-D freehand ultrasound," *Ultrasound in Med. Biol.* **24**(6), 855–869 (1998).

[9] Boctor, E. M., Jain, A., Choti, M. A., Taylor, R. H., and Fichtinger, G., "A rapid calibration method for registration and 3D tracking of ultrasound images using a spatial localizer," in [*SPIE Medical Imaging: Ultrasonic Imaging and Signal Processing*], (2003).

[10] Cleary, K., Cheng, P., Enquobahrie, A., and Yaniv, Z., eds., [*IGSTK: The Book*], Signature Book Printing (2009).

[11] Muratore, D. M. and Galloway, Jr., R. L., "Beam calibration without a phantom for creating a 3-D freehand ultrasound system," *Ultrasound in Med. Biol.* **27**(11), 1557–1566 (2001).

[12] Detmer, P. R., Bashein, G., Hodges, T., Beach, K. W., Filer, E. P., Burns, D. H., and Jr., D. S., "3D ultrasonic image feature localization based on magnetic scanhead tracking: In vitro calibration and validation," *Ultrasound in Med. Biol.* **20**(9), 923 – 936 (1994).

[13] Fischler, M. A. and Bolles, R. C., "Random sample consensus: a paradigm for model fitting with applications to image analysis and automated cartography," *Commun. ACM* **24**(6), 381–395 (1981).

[14] Yaniv, Z., "Random sample consensus (RANSAC) algorithm, a generic implementation," *Insight Journal* **July-December** (2010).

[15] Ibáñez, L., Schroeder, W., Ng, L., and Cates, J., [*The ITK Software Guide*], Kitware Inc., 2 ed.

[16] Björck, Å., [*Numerical Methods for Least Squares Problems*], SIAM, Philadelphia (1996).

[17] Golub, G. H. and Van Loan, C. F., [*Matrix Computations*], Johns Hopkins University Press, Baltimore, MD, USA, 3 ed. (1996).

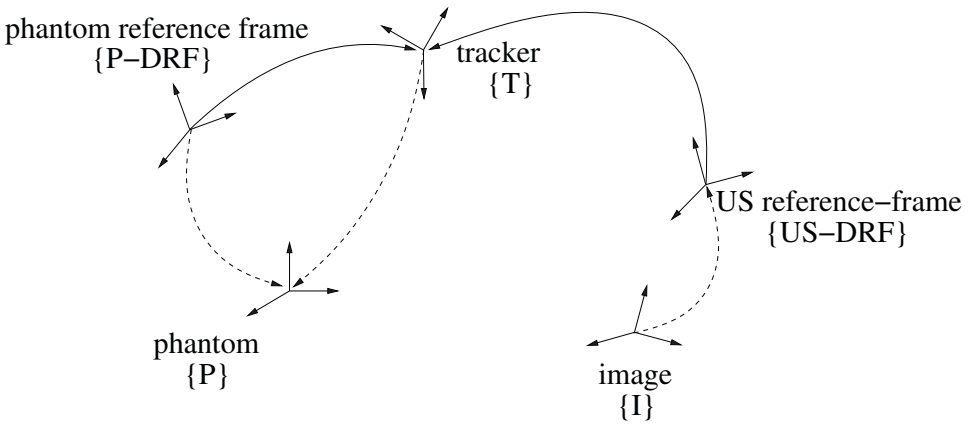

Figure 3. Coordinate systems that potentially play a role in calibration. Solid arrows denote known transformations, dashed denote unknown.

We identify five coordinate systems that potentially play a role in calibration as shown in figure 3, with the phantom's DRF coordinate system being optional.

APPENDIX A. PLANE PHANTOM

The plane phantom is the calibration method that potentially requires the least amount of hardware. That is, to estimate the transformation between the DRF attached to the US probe and the US image coordinate system we only require a water bath with a planar bottom. If the phantom remains stationary throughout the data acquisition process no additional hardware or reference frames are required. Use of planar phantoms designed to improve feature localization in the images is also possible.[7] For additional flexibility with data acquisition a DRF can be attached to the phantom, forgoing the need for a stationary setup.

The derivations bellow follow the convention of identifying the phantom with the x-y plane.

Assuming the phantom remains stationary throughout the data acquisition process we define:

$$
\begin{aligned}
T_1 &\equiv_{\{T\}} T^{\{P\}} \\
T_2 &\equiv_{\{US-DRF\}} T^{\{T\}} \\
T_3 &\equiv_{\{I\}} T^{\{US-DRF\}}
\end{aligned}
$$

Otherwise we define:

$$
\begin{aligned}
T_1 &\equiv_{\{P-DRF\}} T^{\{P\}} \\
T_2 &\equiv_{\{T\}} T^{\{P-DRF\}} \ * \ {}_{\{US-DRF\}}T^{\{T\}} \\
T_3 &\equiv_{\{I\}} T^{\{US-DRF\}}
\end{aligned}
$$

In both cases T_1 and T_2 are rigid transformations. T_3 is an affine transformation, combining both the scaling from image pixels to metric units and the rigid transformation from the image coordinate system to the attached DRF.

The relationship between corresponding points in the plane's coordinate system and the image coordinate system is described by:

$$
\begin{bmatrix} x \\ y \\ 0 \\ 1 \end{bmatrix} = T_1 T_2 T_3 \begin{bmatrix} u \\ v \\ 0 \\ 1 \end{bmatrix} \tag{1}
$$

We consider two parameterizations, a redundant parameterization that leads to an analytic solution and a minimal parameterization that leads to an iterative solution.

A.1 Analytic solution

Using matrices to represent the rigid and affine transformations from equation 1 we use a redundant parameterization, identifying 31 dependent unknowns. Each point contributes a single linear equation of the form:

$$[u_{i,j}R_{2i}(1,:)\ u_{i,j}R_{2i}(2,:)\ u_{i,j}R_{2i}(3,:)\ v_{i,j}R_{2i}(1,:)\ v_{i,j}R_{2i}(2,:)\ v_{i,j}R_{2i}(3,:)\ R_{2i}(1,:)\ R_{2i}(2,:)\ R_{2i}(3,:)\ \mathbf{t_{2i}}\ 1]^T \begin{bmatrix} m_x R_1(3,1)R_3(:,1) \\ m_x R_1(3,2)R_3(:,1) \\ m_x R_1(3,3)R_3(:,1) \\ m_y R_1(3,1)R_3(:,2) \\ m_y R_1(3,2)R_3(:,2) \\ m_y R_1(3,3)R_3(:,2) \\ R_1(3,1)\mathbf{t_3} \\ R_1(3,2)\mathbf{t_3} \\ R_1(3,3)\mathbf{t_3} \\ R_1(3,:) \\ t_{1z} \end{bmatrix} = 0$$

Where $R_c(j,:), R_c(:,j)$ are the j'th row, column, of the rotation matrix associated with transformation T_c, and $[u_{i,j}, v_{i,j}]$ is the j'th image point associated with transformation T_{2i}. Using at least 31 points and ignoring the constraints associated with the rotation matrix entries we obtain the optimal, non-trivial, solution as:

$$\mathbf{x}^* = \arg\min_{\mathbf{x}} \|A\mathbf{x}\| \quad s.t. \|\mathbf{x}\| = 1$$

The optimal solution is obtained as the right singular vector corresponding to the smallest singular value from the singular value decomposition of A.[16] Obviously this solution is not the one we seek as it does not satisfy the constraints associated with the rotation matrix entries. We now enforce these constraints. We first scale the solution by
$\pm\alpha = 1/\sqrt{\mathbf{x}^*(28\ldots30)^T\mathbf{x}^*(28\ldots30)}$. Choice of sign for the scale factor only effects the estimate of T_1 which we will ignore. This modified solution now satisfies the constraint $\|\mathbf{x}^*(28\ldots30)\| = \|R_1(3,:)\| = 1$. To enforce the constraints on R_3 we obtain its first and second columns, as normalized averages of the corresponding first, and second nine entries of $\mathbf{x}^*$. The third column is the cross product of the other two. The resulting matrix does not necessarily represent a rotation, it has unit vector columns but they are not orthogonal. The closest, in the Frobenius norm sense, rotation matrix is obtained via singular value decomposition of this matrix.[17]

A.2 Iterative solution

Using matrices to represent the rigid and affine transformations from equation 1 a minimal parameterization requires 11 independent unknowns, $\mathbf{x} = (\omega 1_y, \omega 1_x, t_{1z}, t_{3x}, t_{3y}, t_{3z}, \omega 3_z, \omega 3_y, \omega 3_x, m_x, m_y)$, with Euler angles representing the rotation. Each point contributes a single nonlinear equation, the signed distance between the point and the x-y plane. The optimal solution is obtained with the Levenberg-Marquardt algorithm as:

$$\mathbf{x}^* = \arg\min_{\mathbf{x}} \sum_k \delta_k^2$$

where

$$
\begin{aligned}
\delta_k \;=\;& -u_{i,j}R_{2i}(1,1)m_x\sin(\omega 1_y)\cos(\omega 3_z)\cos(\omega 3_y)- \\
& u_{i,j}R_{2i}(1,2)m_x\sin(\omega 1_y)\sin(\omega 3_z)\cos(\omega 3_y)+ \\
& u_{i,j}R_{2i}(1,3)m_x\sin(\omega 1_y)\sin(\omega 3_y)+ \\
& u_{i,j}R_{2i}(2,1)m_x\cos(\omega 1_y)\sin(\omega 1_x)\cos(\omega 3_z)\cos(\omega 3_y)+ \\
& u_{i,j}R_{2i}(2,2)m_x\cos(\omega 1_y)\sin(\omega 1_x)\sin(\omega 3_z)\cos(\omega 3_y)- \\
& u_{i,j}R_{2i}(2,3)m_x\cos(\omega 1_y)\sin(\omega 1_x)\sin(\omega 3_y)+ \\
& u_{i,j}R_{2i}(3,1)m_x\cos(\omega 1_y)\sin(\omega 1_x)\cos(\omega 3_z)\cos(\omega 3_y)+ \\
& u_{i,j}R_{2i}(3,2)m_x\cos(\omega 1_y)\sin(\omega 1_x)\sin(\omega 3_z)\cos(\omega 3_y)- \\
& u_{i,j}R_{2i}(3,3)m_x\cos(\omega 1_y)\sin(\omega 1_x)\sin(\omega 3_y)- \\
& v_{i,j}R_{2i}(1,1)m_y\sin(\omega 1_y)(\cos(\omega 3_z)\sin(\omega 3_y)\sin(\omega 3_x)-\sin(\omega 3_z)\cos(\omega 3_x))- \\
& v_{i,j}R_{2i}(1,2)m_y\sin(\omega 1_y)(\sin(\omega 3_z)\sin(\omega 3_y)\sin(\omega 3_x)+\cos(\omega 3_z)\cos(\omega 3_x))- \\
& v_{i,j}R_{2i}(1,3)m_y\sin(\omega 1_y)\cos(\omega 3_y)\sin(\omega 3_x)+ \\
& v_{i,j}R_{2i}(2,1)m_y\cos(\omega 1_y)\sin(\omega 1_x)(\cos(\omega 3_z)\sin(\omega 3_y)\sin(\omega 3_x)-\sin(\omega 3_z)\cos(\omega 3_x))+ \\
& v_{i,j}R_{2i}(2,2)m_y\cos(\omega 1_y)\sin(\omega 1_x)(\sin(\omega 3_z)\sin(\omega 3_y)\sin(\omega 3_x)+\cos(\omega 3_z)\cos(\omega 3_x))+ \\
& v_{i,j}R_{2i}(2,3)m_y\cos(\omega 1_y)\sin(\omega 1_x)\cos(\omega 3_y)\sin(\omega 3_x)+ \\
& v_{i,j}R_{2i}(3,1)m_y\cos(\omega 1_y)\sin(\omega 1_x)(\cos(\omega 3_z)\sin(\omega 3_y)\sin(\omega 3_x)-\sin(\omega 3_z)\cos(\omega 3_x))+ \\
& v_{i,j}R_{2i}(3,2)m_y\cos(\omega 1_y)\sin(\omega 1_x)(\sin(\omega 3_z)\sin(\omega 3_y)\sin(\omega 3_x)+\cos(\omega 3_z)\cos(\omega 3_x))+ \\
& v_{i,j}R_{2i}(3,3)m_y\cos(\omega 1_y)\sin(\omega 1_x)\cos(\omega 3_y)\sin(\omega 3_x)- \\
& R_{2i}(1,1)\sin(\omega 1_y)t_{3x}- \\
& R_{2i}(1,2)\sin(\omega 1_y)t_{3y}- \\
& R_{2i}(1,3)\sin(\omega 1_y)t_{3z}+ \\
& R_{2i}(2,1)\cos(\omega 1_y)\sin(\omega 1_x)t_{3x}+ \\
& R_{2i}(2,2)\cos(\omega 1_y)\sin(\omega 1_x)t_{3y}+ \\
& R_{2i}(2,3)\cos(\omega 1_y)\sin(\omega 1_x)t_{3z}+ \\
& R_{2i}(3,1)\cos(\omega 1_y)\sin(\omega 1_x)t_{3x}+ \\
& R_{2i}(3,2)\cos(\omega 1_y)\sin(\omega 1_x)t_{3y}+ \\
& R_{2i}(3,3)\cos(\omega 1_y)\sin(\omega 1_x)t_{3z}- \\
& t_{2x}\sin(\omega 1_y)+ \\
& t_{2y}\cos(\omega 1_y)\sin(\omega 1_x)+ \\
& t_{2z}\cos(\omega 1_y)\cos(\omega 1_x)+ \\
& t_{1z}
\end{aligned}
$$

APPENDIX B. POINTER AND CROSS-WIRE PHANTOM

The pointer and cross-wire calibration methods are based on imaging a point target, either the intersection of the cross wires or the pointer tip. Mathematically the two methods are all but equivalent, with the cross-wire approach requiring the estimation of three additional parameters.

B.1 Pointer based calibration

Using a calibrated pointer we know the translation from the pointer's DRF to its tip. Using the coordinate systems shown in figure 3, we define:

$$T_2 \equiv_{\{US-DRF\}} T^{\{T\}}$$
$$T_3 \equiv_{\{I\}} T^{\{US-DRF\}}$$

T_2 is a rigid transformation and T_3 is an affine transformation, combining both the scaling from image pixels to metric units and the rigid transformation from the image coordinate system to the attached DRF.

The relationship between corresponding points in the tracker's coordinate system and the image coordinate system is described by:

$$\begin{bmatrix} x \\ y \\ z \\ 1 \end{bmatrix} = T_2 T_3 \begin{bmatrix} u \\ v \\ 0 \\ 1 \end{bmatrix} \tag{2}$$

We consider two parameterizations, a redundant parameterization that leads to an analytic solution and a minimal parameterization that leads to an iterative solution.

B.1.1 Analytic solution

Using matrices to represent the rigid and affine transformations from equation 2 we use a redundant parameterization, identifying nine dependent unknowns. Each point contributes three linear equation of the form:

$$[u_i R_{2i}\ v_i R_{2i}\ R_{2i}] \begin{bmatrix} m_x R_3(:,1) \\ m_y R_3(:,2) \\ \mathbf{t_3} \end{bmatrix} = [\mathbf{p}_i - \mathbf{t_{2i}}]$$

where $\mathbf{p}_i$ is the pointer tip's location in the tracker's coordinate system.

Using at least three points and ignoring the constraints associated with the rotation matrix entries we obtain the optimal solution as:

$$\mathbf{x}^* = \arg\min_{\mathbf{x}} \|A\mathbf{x} - b\|$$

The optimal solution corresponds to the solution of the equation system $A\mathbf{x} = b$ which is obtained using the pseudo-inverse. To enforce the constraints on R_3 we obtain its first and second columns, by normalizing the first and second triplet of entries in $\mathbf{x}^*$. The third column is the cross product of the other two. The resulting matrix is not necessarily a rotation. The closest, in the Frobenius norm sense, rotation matrix is obtained via singular value decomposition of this matrix.[17]

B.2 Iterative solution

Using matrices to represent the rigid and affine transformations from equation 2 a minimal parameterization requires 8 independent unknowns, $\mathbf{x} = (t_{3x}, t_{3y}, t_{3z}, \omega 3_z, \omega 3_y, \omega 3_x, m_x, m_y)$, with Euler angles representing the rotation. Each point contributes one nonlinear equation. The optimal solution is obtained with the Levenberg-Marquardt algorithm as:

$$\mathbf{x}^* = \arg\min_{\mathbf{x}} \sum_k \delta_k^2$$

where

$$\begin{aligned}
\delta_k^2 \;=\; & [A(1,1)m_x \cos(\omega 3_z)\cos(\omega 3_y) + A(1,2)m_x \sin(\omega 3_z)\cos(\omega 3_y) - A(1,3)m_x \sin(\omega 3_y) + \\
& A(1,4)m_y(\cos(\omega 3_z)\sin(\omega 3_y)\sin(\omega 3_x) - \sin(\omega 3_z)\cos(\omega 3_x)) + \\
& A(1,5)m_y(\sin(\omega 3_z)\sin(\omega 3_y)\sin(\omega 3_x) + \cos(\omega 3_z)\cos(\omega 3_x)) + \\
& A(1,6)m_y \cos(\omega 3_y)\sin(\omega 3_x) + A(1,7)t_{3x} + A(1,8)t_{3y} + A(1,9)t_{3z} - b_1]^2 + \\
& [A(2,1)m_x \cos(\omega 3_z)\cos(\omega 3_y) + A(2,2)m_x \sin(\omega 3_z)\cos(\omega 3_y) - A(2,3)m_x \sin(\omega 3_y) + \\
& A(2,4)m_y(\cos(\omega 3_z)\sin(\omega 3_y)\sin(\omega 3_x) - \sin(\omega 3_z)\cos(\omega 3_x)) + \\
& A(2,5)m_y(\sin(\omega 3_z)\sin(\omega 3_y)\sin(\omega 3_x) + \cos(\omega 3_z)\cos(\omega 3_x)) + \\
& A(2,6)m_y \cos(\omega 3_y)\sin(\omega 3_x) + A(2,7)t_{3x} + A(2,8)t_{3y} + A(2,9)t_{3z} - b_2]^2 + \\
& (A(3,1)m_x \cos(\omega 3_z)\cos(\omega 3_y) + A(3,2)m_x \sin(\omega 3_z)\cos(\omega 3_y) - A(3,3)m_x \sin(\omega 3_y) + \\
& A(3,4)m_y(\cos(\omega 3_z)\sin(\omega 3_y)\sin(\omega 3_x) - \sin(\omega 3_z)\cos(\omega 3_x)) + \\
& A(3,5)m_y(\sin(\omega 3_z)\sin(\omega 3_y)\sin(\omega 3_x) + \cos(\omega 3_z)\cos(\omega 3_x)) + \\
& A(3,6)m_y \cos(\omega 3_y)\sin(\omega 3_x) + A(3,7)t_{3x} + A(3,8)t_{3y} + A(3,9)t_{3z} - b_3)^2
\end{aligned}$$

B.3 Cross-wire based calibration

Using a cross-wire phantom and the coordinate systems shown in figure 3, we either assume the phantom is stationary throughout the data acquisition or we attach a DRF to it.

In the former case we define:

$$T_1 \equiv_{\{P\}} T^{\{T\}}$$
$$T_2 \equiv_{\{US-DRF\}} T^{\{T\}}$$
$$T_3 \equiv_{\{I\}} T^{\{US-DRF\}}$$

while in the latter we define:

$$T_1 \equiv_{\{P\}} T^{\{P-DRF\}}$$
$$T_2 \equiv_{\{T\}} T^{\{P-DRF\}} * {}_{\{US-DRF\}}T^{\{T\}}$$
$$T_3 \equiv_{\{I\}} T^{\{US-DRF\}}$$

As our phantom consists of a single point we can arbitrarily choose its reference frame's orientation. We thus set it to the identity. As a result T_1 represents a 3D translation, T_2 is a rigid transformation, and T_3 is an affine transformation, combining both the scaling from image pixels to metric units and the rigid transformation from the image coordinate system to the attached DRF.

The relationship between corresponding points is described by:

$$T_1 \begin{bmatrix} 0 \\ 0 \\ 0 \\ 1 \end{bmatrix} = \begin{bmatrix} \mathbf{t_1} \\ 1 \end{bmatrix} = T_2 T_3 \begin{bmatrix} u \\ v \\ 0 \\ 1 \end{bmatrix} \tag{3}$$

We consider two parameterizations, a redundant parameterization that leads to an analytic solution and a minimal parameterization that leads to an iterative solution.

B.3.1 Analytic solution

Using matrices to represent the rigid and affine transformations from equation 3 we use a redundant parameterization, identifying 12 dependent unknowns. Each point contributes three linear equation of the form:

$$[u_i R_{2i}\ v_i R_{2i}\ R_{2i} - I] \begin{bmatrix} m_x R_3(:,1) \\ m_y R_3(:,2) \\ \mathbf{t_3} \\ \mathbf{t_1} \end{bmatrix} = [-\mathbf{t_{2i}}]$$

Using at least four points and ignoring the constraints associated with the rotation matrix entries we obtain the optimal solution as:

$$\mathbf{x}^* = \arg\min_{\mathbf{x}} \|A\mathbf{x} - b\|$$

The solution is obtained in the same manner as in the pointer based calibration.

B.3.2 Iterative solution

Using matrices to represent the rigid and affine transformations from equation 3 a minimal parameterization requires 11 independent unknowns, $\mathbf{x} = (t_{1x}, t_{1y}, t_{1z}, t_{3x}, t_{3y}, t_{3z}, \omega 3_z, \omega 3_y, \omega 3_x, m_x, m_y)$, with Euler angles representing the rotation. Each point contributes one nonlinear equation. The optimal solution is obtained with the Levenberg-Marquardt algorithm as:

$$\mathbf{x}^* = \arg\min_{\mathbf{x}} \sum_k \delta_k^2$$

where

$$\begin{aligned}
\delta_k^2 \;=\; & [A(1,1)m_x \cos(\omega 3_z)\cos(\omega 3_y) + A(1,2)m_x \sin(\omega 3_z)\cos(\omega 3_y) - A(1,3)m_x \sin(\omega 3_y) + \\
& A(1,4)m_y(\cos(\omega 3_z)\sin(\omega 3_y)\sin(\omega 3_x) - \sin(\omega 3_z)\cos(\omega 3_x)) + \\
& A(1,5)m_y(\sin(\omega 3_z)\sin(\omega 3_y)\sin(\omega 3_x) + \cos(\omega 3_z)\cos(\omega 3_x)) + \\
& A(1,6)m_y \cos(\omega 3_y)\sin(\omega 3_x) + A(1,7)t_{3x} + A(1,8)t_{3y} + A(1,9)t_{3z} - t_{1x} - b_1]^2 + \\
& [A(2,1)m_x \cos(\omega 3_z)\cos(\omega 3_y) + A(2,2)m_x \sin(\omega 3_z)\cos(\omega 3_y) - A(2,3)m_x \sin(\omega 3_y) + \\
& A(2,4)m_y(\cos(\omega 3_z)\sin(\omega 3_y)\sin(\omega 3_x) - \sin(\omega 3_z)\cos(\omega 3_x)) + \\
& A(2,5)m_y(\sin(\omega 3_z)\sin(\omega 3_y)\sin(\omega 3_x) + \cos(\omega 3_z)\cos(\omega 3_x)) + \\
& A(2,6)m_y \cos(\omega 3_y)\sin(\omega 3_x) + A(2,7)t_{3x} + A(2,8)t_{3y} + A(2,9)t_{3z} - t_{1y} - b_2]^2 + \\
& (A(3,1)m_x \cos(\omega 3_z)\cos(\omega 3_y) + A(3,2)m_x \sin(\omega 3_z)\cos(\omega 3_y) - A(3,3)m_x \sin(\omega 3_y) + \\
& A(3,4)m_y(\cos(\omega 3_z)\sin(\omega 3_y)\sin(\omega 3_x) - \sin(\omega 3_z)\cos(\omega 3_x)) + \\
& A(3,5)m_y(\sin(\omega 3_z)\sin(\omega 3_y)\sin(\omega 3_x) + \cos(\omega 3_z)\cos(\omega 3_x)) + \\
& A(3,6)m_y \cos(\omega 3_y)\sin(\omega 3_x) + A(3,7)t_{3x} + A(3,8)t_{3y} + A(3,9)t_{3z} - t_{1z} - b_3)^2
\end{aligned}$$